ACS NANO

www.acsnano.org

ARTICLE

Ultrafast Electron Microscopy of Nanoscale Charge Dynamics in Semiconductors

Michael Yannai, Raphael Dahan, Alexey Gorlach, Yuval Adiv, Kangpeng Wang, Ivan Madan, Simone Gargiulo, Francesco Barantani, Eduardo J. C. Dias, Giovanni Maria Vanacore, Nicholas Rivera, Fabrizio Carbone, F. Javier García de Abajo, and Ido Kaminer*

Cite This: *ACS Nano* 2023, 17, 3645−3656

Read Online

ACCESS | Metrics & More | Article Recommendations | Supporting Information

ABSTRACT: **The ultrafast dynamics of charge carriers in solids plays a pivotal role in emerging optoelectronics, photonics, energy harvesting, and quantum technology applications. However, the investigation and direct visualization of such nonequilibrium phenomena remains as a long-standing challenge, owing to the nanometer-femtosecond spatiotemporal scales at which the charge carriers evolve. Here, we propose and demonstrate an interaction mechanism enabling nanoscale imaging of the femtosecond dynamics of charge carriers in solids. This imaging modality, which we name charge dynamics electron microscopy (CDEM), exploits the strong interaction of free-electron pulses with terahertz (THz) near fields produced by the moving charges in an ultrafast scanning transmission electron microscope. The measured free-electron energy at different spatiotemporal coordinates allows us to directly retrieve the THz near-field amplitude and phase, from which we reconstruct movies of the generated charges by comparison to microscopic theory. The CDEM technique thus allows us to investigate previously inaccessible spatiotemporal regimes of charge dynamics in solids, providing insight into the photo-Dember effect and showing oscillations of photogenerated electron−hole distributions inside a semiconductor. Our work facilitates the exploration of a wide range of previously inaccessible charge-transport phenomena in condensed matter using ultrafast electron microscopy.**

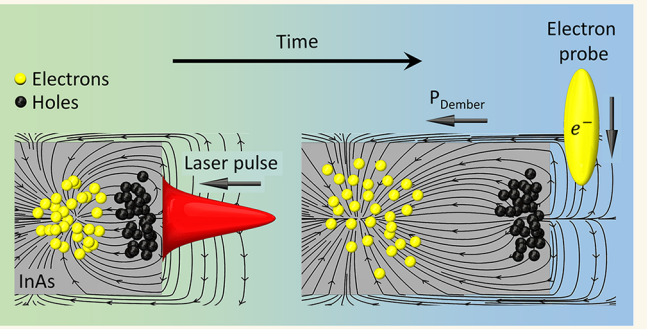

KEYWORDS: *ultrafast charge transport, electron−hole dynamics, terahertz near field imaging, terahertz spectroscopy, terahertz emission, ultrafast electron microscopy, Dember effect*

At the heart of many solid-state physics phenomena of current interest is the intriguing ultrafast dynamics of charge carriers and their various hybrid states. Different approaches for imaging ultrafast charge dynamics[1] aim to provide insights in diverse fields such as superconductivity, magnetoresistance, and plasma formation. Many of these phenomena occur on a picosecond time scale, owing to the underlying physics having THz-frequency resonances, as well as meV binding and quasiparticle energies. Imaging the ultrafast charge dynamics involved in these phenomena necessitates powerful microscopy capabilities that combine a sufficient resolution in space (nanometer-scale) and time (subpicosecond-scale) along with other observables such as energy and momentum.

Here, we propose and demonstrate an interaction mechanism that enables imaging of ultrafast charge dynamics by inelastic scattering of free-electron-pulse probes in an electron microscope. The inelastic interaction between electron pulses and charge carriers is mediated by time-dependent THz-frequency near fields emitted following picosecond time scale motion of the charge carriers in the bulk of a photoexcited material. This interaction enables the reconstruction of the charge dynamics with nanometer spatial resolution and subpicosecond temporal precision without perturbing it by the external free-electron probe. We present an experimental demonstration of this concept and develop a broadly applicable theory in excellent agreement with our measurements.

Currently available microscopy techniques for imaging nanoscale charge dynamics rely on either optical excitation

Received: October 20, 2022
Accepted: January 27, 2023
Published: February 3, 2023

https://doi.org/10.1021/acsnano.2c10481
ACS Nano 2023, 17, 3645−3656

and detection[2−5] or analysis of electron emission from the surface.[6−13] Several specific implementations rely on measurements of THz near fields scattered by or generated from the surface, enabling the reconstruction of picosecond and submicron charge dynamics.[14−16] Complementary approaches include ultrafast electron diffraction (UED),[17−20] which provides momentum-space information on charge dynamics in the bulk, as well as ultrafast point-projection electron microscopy (UPEM) with a spatial resolution of tens of nanometers using low-energy (few-hundreds of eVs) electrons.[21−24] Of particular importance in the context of the current work is the study by Müller et al.,[22] which used UPEM to investigate ultrafast electric currents in axially doped InP NWs, and those of Vogelsang et al.[23] and Hergert et al.,[24] which studied ultrafast electron photoemission from a nanogap antenna using UPEM. In the latter, the authors analyze the effect of transient electric fields induced by the photoemitted electrons on the kinetic energy distributions of the probe electrons. Another notable approach involves mapping of static charge and field distributions from elastic electron scattering.[25,26] Furthermore, charge dynamics associated with the linear optical response of micron-scale metallic resonators has been probed under external THz irradiation using ultrafast electron deflectometry.[27] This technique has also been applied to the study of plasma formation and its subsequent free-space evolution in the picosecond and nanosecond time-scales.[28,29] Such advances emphasize the potential of free-electron pulses to explore charge-carrier dynamics.

Ultrafast electron imaging experiments are made possible by the invention and swift development of the ultrafast transmission electron microscope (UTEM)[30,31]—a pump−probe setup that uses femtosecond laser pulses to excite a sample and synchronized femtosecond electron pulses to measure the resulting transient state. Previous studies have utilized UTEMs to capture the dynamics of electromagnetic fields in various nanoscale and low-dimensional structures: imaging the evolution of plasmons in metallic nanostructures[32] and buried interfaces,[33] confined modes in optical cavities,[34,35] the accelerating field in silicon-photonic dielectric laser accelerators,[36] phonon[37] and polariton wavepackets in 2D materials,[38] and phase transitions[39,40] and Skyrmion dynamics.[41]

These previous UTEM experiments relied on the interaction of the electron beam with optical fields at the light excitation frequency, to which the investigated specimen responded linearly. In contrast, in this work we present a direct demonstration of a strongly nonlinear optical interaction within the UTEM. Specifically, our experiment measures the THz field created by moving charge carriers, which are generated via optical-frequency excitation of a bulk InAs crystal—the so-called photo-Dember effect.[42] We thus demonstrate free-electron-based near-field imaging of an *in situ* generated THz field, revealing information about the THz generation process and elucidating its spatiotemporal dynamics. The field measurement is based on the position- and time-dependent energy shift of the probe electron in response to its interaction with the THz field. In this manner, the electron maps the field in both space and time. We further utilize this near-field mapping to reconstruct the underlying charge distribution (i.e., the time-evolving carrier density inside the material) that drives the process. The reconstructed charge distribution reveals previously inaccessible aspects of the spatiotemporal evolution of electron and hole densities at the heart of the photo-Dember effect.

We name the demonstrated ultrafast imaging technique *charge dynamics electron microscopy* (CDEM) and develop the theoretical framework describing the electron−field interaction that lies at the core of CDEM, supporting the exploration of ultrafast solid-state charge transport phenomena. This framework encompasses a broad class of interactions between free-electron pulses and charge carriers, where the interaction occurs via the fields produced by the charge dynamics. We show that CDEM can capture instantaneous local electric field distributions with amplitudes as low as 10^3 V/m in our current setup, and can reach the range of 10 V/m using better electron energy spectrometers that are already commercially available.[43]

Being a TEM-based approach, CDEM holds the potential to sense internal fields buried inside a bulk sample, using the electron penetration into the bulk (up to ∼100 nm) in a nondestructive manner. In this way, CDEM differs from other near-field approaches (e.g., based on sharp scanning tips) that probe the field near the sample surface. CDEM thus facilitates the observation of a variety of fascinating, previously inaccessible condensed-matter phenomena. For example, we envision the visualization of ultrafast low-temperature superconducting phase transitions, quantum resistivity oscillations, ultrafast metal−insulator transitions, and much more. These effects occur on a subpicosecond time scale and display nanometer-scale features, making CDEM an appealing approach for their direct observation. Our experiment presents initial promising steps toward the realization of such ambitious goals.

RESULTS

Figure 1A describes the interaction mechanism that enables the reconstruction of nanoscale-resolved charge dynamics using free-electron pulses (see Methods and theory in the Supporting Information (SI) for details). We demonstrate this interaction using a 60-μm-thick p-type InAs crystal with (111) growth orientation (see Methods for details), which is positioned inside the UTEM with a cleaved {110} facet facing the pump laser beam. The latter consists of IR pump pulses impinging the InAs crystal at time t_0 (Figure 1A, top panel), inducing transient electron and hole currents. Owing to the photo-Dember effect,[42] the highly mobile photoexcited electrons rapidly diffuse toward the bulk of the crystal, while the less mobile holes (electron−hole mobility ratio $\mu_e/\mu_h \approx 100$) remain mostly confined near the surface. Diffusion and drift forces lead to picosecond time scale variations in the velocity- and charge-densities of the two types of charge carriers. As a result, a THz-frequency near field is generated around the charges, and propagates away from the crystal as a THz pulse.

An electron pulse moving along z arrives at a time delay Δt after t_0 and passes by the vicinity of the pumped crystal face at a lateral distance (impact parameter) x and lateral offset y (Figure 1A, bottom panel). As illustrated in Figures 1B and C, the THz field changes significantly while the electron passes through the interaction region, resulting in a net energy shift of the electron, measured by using an electron energy-loss spectrometer (EELS). For instance, the electron labeled $\Delta t_2 = 0$ in Figure 1B sees no field at $z < 0$ and only positive fields at $z > 0$, and consequently, it decelerates. In contrast, the electron identified by the label $\Delta t_3 = 0.6$ ps, experiences an overall acceleration. Even an electron that arrives at a negative time delay ($\Delta t_1 = -0.24$ ps) can still undergo a nonzero energy shift

https://doi.org/10.1021/acsnano.2c10481
ACS Nano 2023, 17, 3645−3656

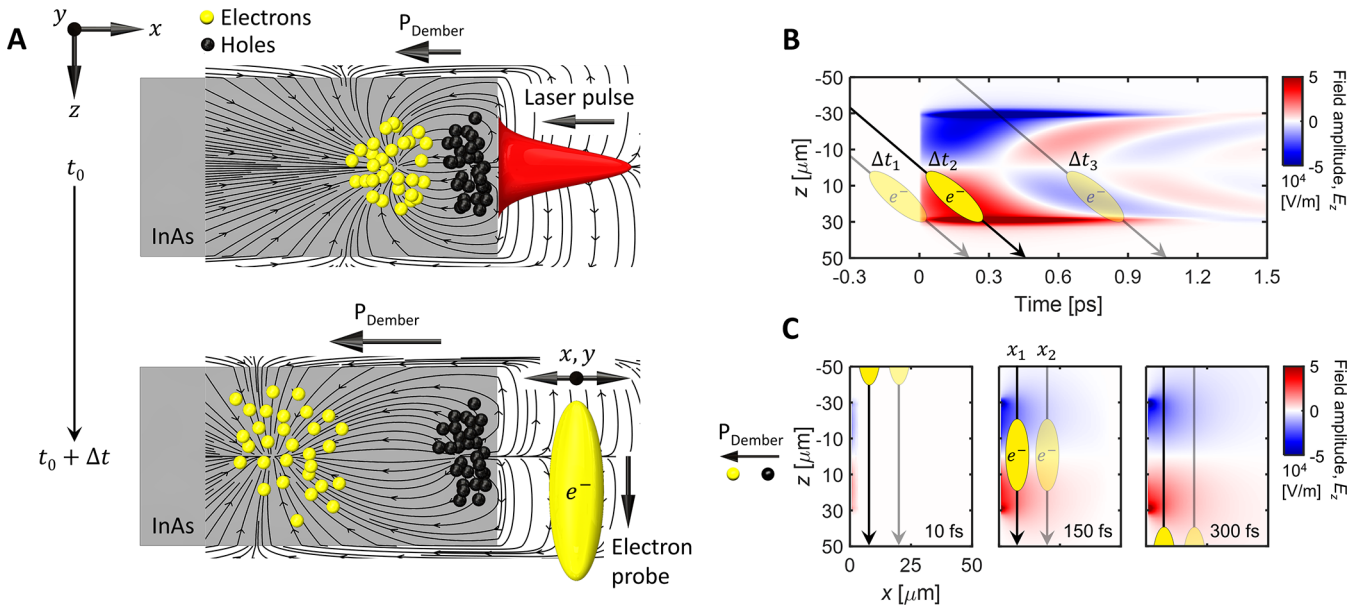

Figure 1. Probing near-field THz generation using charge dynamics electron microscopy (CDEM). (A) Illustration of THz pulse generation via the photo-Dember effect and subsequent measurement by a free-electron pulse. Top panel: An IR laser pulse (red, 40 μm diameter, 50 fs duration, 800 nm central wavelength) impinges from the right at time t_0 on an InAs crystal (gray). The IR light generates transient electron and hole currents (yellow and black circles, respectively), which lead to the emission of THz-frequency electromagnetic radiation (black electric field lines). Bottom panel: A time-delayed electron pulse (yellow ellipse, 200 keV energy) passes by the vicinity of the crystal and undergoes an energy shift (0.1 eV spectrometer resolution) under the influence of the emitted radiation. (B) Simulated electric field z-component amplitude (E_z) versus time and position along the z coordinate (evaluated 1 μm away from the crystal face). (C) Simulated xz-plane cross-sections of E_z at several time delays. Yellow ellipses in (B) and (C) illustrate the electron trajectories (velocity $v = 0.7c$) inside the electric field at different time delays Δt_{1-3} (marked in the corresponding panels of Figure 2B), and at different positions x_{1-2}, respectively. Data in (B) and (C) are evaluated at the plane of pump laser incidence and correspond to a pump-laser pulse energy of 10 nJ, with the color bar having 30% saturation for better visibility.

due to the extended interaction region and electron-pulse duration.

We raster-scan the electron position in the xy plane by measuring in scanning-transmission-electron-microscopy (STEM) mode, collecting the electron energy spectrum at each point (see Methods for details). The spatial resolution in the xy plane is determined by the raster pitch and the electron beam spot size: 1 μm in Figure 2A, and 50 nm in Figure 2C. Much smaller spot sizes can be configured in many existing state-of-the-art electron microscopes, only limited by the field-of-view and the thickness of the sample over which the electron beam remains collimated. Moreover, our results below show that the reconstructed charge dynamics can exhibit spatial features much smaller than the spatial resolution of the measurement.

Each electron integrates the E_z component of the field along its trajectory (see theory in the SI), yielding a time-dependent electron energy distribution from which the integrated field can be extracted. Since the THz field is just single-cycle to a few-cycles long, we can effectively map both its phase and amplitude (see theory in the SI). We note that the lateral components of the THz near field (E_x and E_y) are also accessible through local measurements of the electron deflection in the diffraction plane. The entire vector field $\boldsymbol{E}(x,y,z,t)$ could in-principle be obtained using a tomographic reconstruction by a sequence of measurements for different sample tilt angles.

We investigated the electron–field interaction using several sample geometries, and focus the results presented in the figures on a triangle-shaped specimen (Figure 2), naturally formed when the (111)-grown InAs crystal is cleaved along the {110} facets. This geometry allows us to observe the field pattern emitted from both the excited and unexcited edges, providing information on the spatially resolved phase of the emitted THz pulse. The internal charge distribution oscillates, forming an x-oriented THz dipole having a π-shifted phase on opposite sides of the sample. This behavior is exhibited in the measured spatiotemporal maps (xy plane) of the average electron energy shifts $\Delta\varepsilon$ around the triangle-shaped InAs crystal, shown in Figure 2A for various pump–probe time delays. Figure 2B shows the corresponding simulations, which agree well with the measured data. Additional measurements are presented in Figure S2, showing larger-field-of-view maps taken near a straight-edge crystal (the complete measurements of the field dynamics are presented in Movies S1 and S2).

The insets in Figure 2B show xy-plane cross-sections of the reconstructed charge distributions at the corresponding points in time. Figure 3 shows enlarged panels of the charge distributions, as well as yz-plane cross-sections. The smallest features that can be identified in these reconstructed distributions are ~100 nm, as evidenced by the width of the oscillatory charge distribution. Movie S3 combines both cross-sections to show the complete reconstructed dynamics. The energy shifts in Figure 2A are nonzero at negative time delays due to the prolonged interaction with the electron pulse (~350 fs duration), as shown in Figure 1B, enabling the electron to sense the THz field produced by a pump pulse arriving a fraction of a picosecond earlier. Nevertheless, the reconstructed instantaneous charge distributions presented in the insets are zero at negative times, as expected from the short interaction with the excitation pulse (50 fs duration).

https://doi.org/10.1021/acsnano.2c10481
ACS Nano 2023, 17, 3645–3656

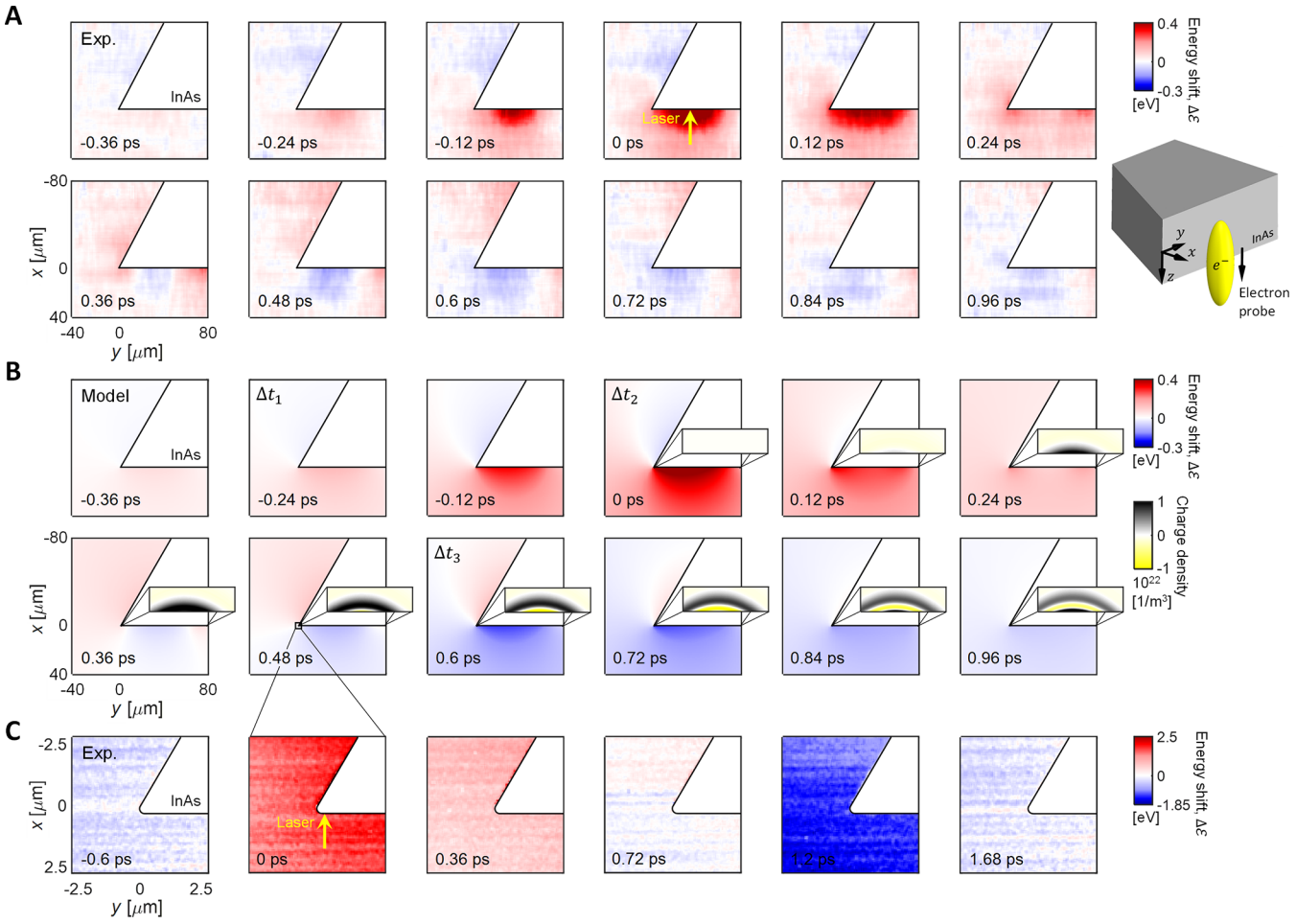

Figure 2. Spatiotemporal charge distribution reconstruction via near-field mapping of the THz field. (A) Measured spatiotemporal maps of electron-beam energy shifts. These maps display the mean electron energy shift $\Delta\varepsilon$ produced by scanning the electron position in the *xy* plane at various time delays (see labels), thus rendering the THz pulse spatiotemporal dynamics. The pump laser pulse is incident along the *x* axis, normal to the crystal surface, 30 μm away from the tip along *y* and at the center of the crystal with respect to *z*, as illustrated by the yellow arrow in the 0 ps panel. The spatial resolution in these measurements of the THz field is dictated by the 1 μm spot size of the probe electron. The right inset provides a three-dimensional illustration of the sample geometry (gray), the electron pulse (yellow), and the axes system. (B) Simulated energy shift $\Delta\varepsilon$ corresponding to the experimental data in (A). Insets depict the electron−hole charge distribution reconstructed from the measurements. The cross-sections of the charge distribution are taken at the $z = 0$ plane. Insets span 600 nm (80 μm) along *x* (*y*), revealing spatial features of ∼100 nm scale in the charge distribution. Labels Δt_{1-3} in (B) refer to the time delays indicated in Figure 1B. (C) Measured spatiotemporal maps of electron-beam energy shifts, focusing on the InAs crystal tip (5 × 5 μm^2 region), with probe electron spot size of 50 nm. The pump laser pulse is incident along the *x* axis, normal to the crystal surface and centered at the tip ($x,y,z = 0$), as illustrated by the yellow arrow in the 0 ps panel. All data displayed refer to a pump-laser pulse energy of 10 nJ, with the color bars having 30% saturation for better visibility.

Figure 2C shows measured spatiotemporal maps of electron-beam energy shifts, focusing on a smaller 5 × 5 μm^2 region around the InAs crystal tip. The entire data set is displayed in Figure S3. Using a smaller field-of-view and further thinning the crystal to 20 μm (along *z*) allows us to probe the THz near field with a spatial resolution of 50 nm, dictated by the average electron spot size along the interaction region and the chosen raster pitch (both are 50 nm). One can see that the measured electron energy shift is about six times larger than that of Figures 2A and B. This is attributed to the strong THz field confinement at the tip (also seen in Figures 2A,B) further enhanced by positioning the pump laser at the tip. Moreover, the smaller electron probe used in this measurement implies that the electron averages over a smaller region in the lateral plane, thereby increasing its sensitivity. Another evident feature is the slower oscillation of the THz field compared to the that of Figures 2A and B (about a factor 2 slower). This is again explained by the THz field confinement at the tip (also seen in Figures 2A and B), where the crystal geometry confines the field, thereby decreasing its oscillation frequency at the THz range.

From the measured THz field patterns outside the sample, we reconstruct the charge dynamics inside the sample. As with other techniques, such a spatiotemporal reconstruction requires enforcing several constraints on the charge dynamics inside the sample. These constraints enable a unique solution to be obtained from electron measurements outside the crystal volume. In the present instance, sufficient constraints are provided by the use of a hydrodynamic model for the photo-Dember effect,[44] which prescribes the transient currents inside the sample following photoexcitation by the pump laser (eq S17). The Poisson equation is subsequently employed to evaluate the associated scalar potential distribution in space and time (eqs S25−S26). This potential can then be

https://doi.org/10.1021/acsnano.2c10481
ACS Nano 2023, 17, 3645−3656

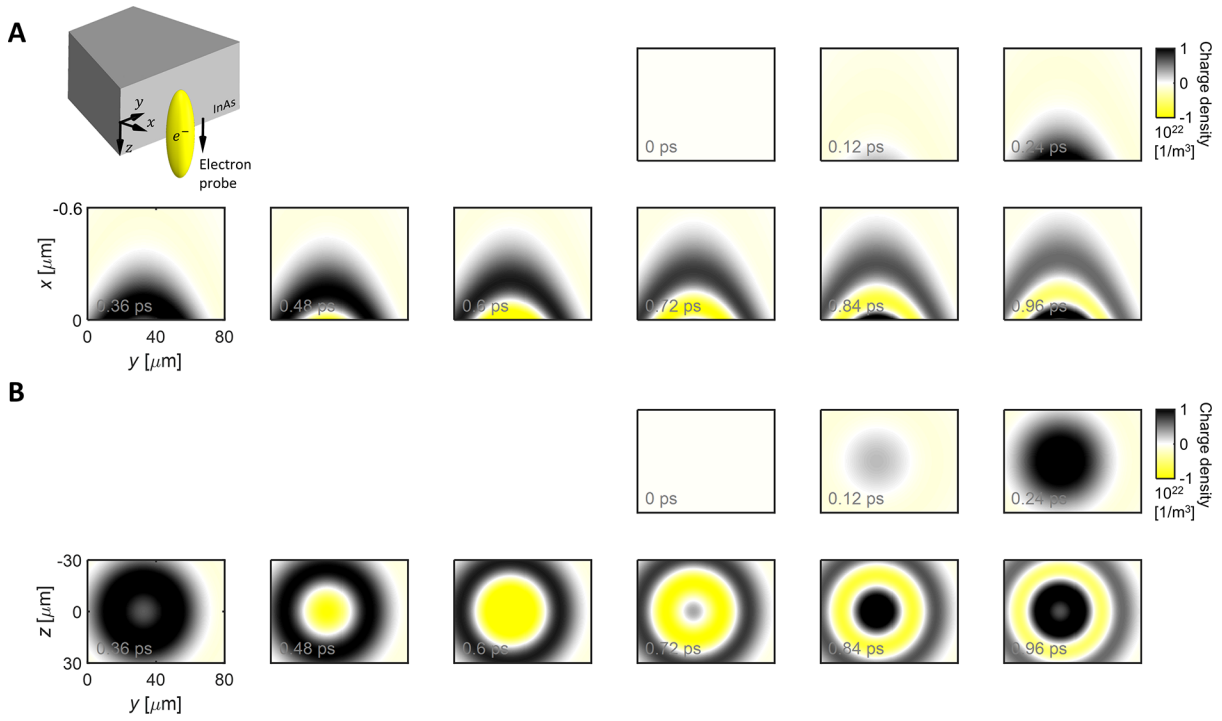

Figure 3. Spatiotemporal evolution of the reconstructed charge density. Cross-sections of the reconstructed charge density in the (A) *xy* plane ($z = 0$) and (B) *yz* plane ($x = 0$). The data in (A) provides an enlarged view of the data presented in the insets of Figure 2B. For clarity, the panels in (A) and (B) are arranged in a similar manner to Figure 2B. Note that the origin of axes is located at the tip of the triangle-shaped sample (shown both in the 3D inset in (A) and in Figure S1). As in Figures 2A and B, the pump laser pulse is incident along the *x* axis, normal to the crystal surface, 30 μm away from the tip along *y*, and at the center of the crystal with respect to *z*.

differentiated to obtain the electric field component along the propagation axis of the probe electron (E_z), which is responsible for any energy change of the latter. Using a classical treatment of the probe electron dynamics (which is more intuitive than the quantum-mechanical one, yet adequate under the conditions of the current work), we can evaluate the electron energy shift through the classical work done by the Lorentz force (eq S17). This requires to integrate the electric field along the electron trajectory for different pump−probe time delays and spatial coordinates. It is therefore understood that the connection between the two entities, the observable, which is the probe electron energy shift, and the reconstructed charge dynamics, requires some delicate treatment to be uncovered, which is however not uncommon for such techniques.

The reconstruction of the THz pulse and underlying charge dynamics is done by fitting this theory to the measured five-dimensional data set that is generated by capturing the entire electron energy spectrum as a function of time delay for different *xy* plane positions and pump pulse energies (see theory in the SI). Specifically, for each set of fitting parameters, we evaluate the transient current density j_x inside the sample. This current density is used to calculate the scalar potential distribution in space and time, and finally the resulting electron spectrum following the interaction. The obtained spectra are compared against the experimental five-dimensional data set, and the process is repeated until the fit satisfies the predefined convergence criteria. Using this approach, we are able to reconstruct the features observed in the experiment with only four fitting parameters, which are found once and for all the recorded data. For this reason, we believe that our simulations adequately reproduce the actual charge distribution generated inside the structure.

Applying CDEM to other (perhaps less well understood) physical systems can be achieved in a similar manner to the current study, assuming that the system under study is not a complete "black-box" and that reasonable assumptions on its behavior can be made. Being a near-field technique, CDEM is sensitive to the microscopic details of the sampled system. Therefore, capturing multidimensional data of sufficient extent should allow one to provide supporting evidence or disprove the validity of a certain model. Determining the validity of a given model can be achieved by examining the effect of perturbations in the fitting parameters on the fit quality. In our experiment, changing the fitting parameters to a level of ±1% yielded no significant change in the reconstructed charge distribution and the resulting fit quality.

We attribute the observed discrepancy between model and experiment at time delays $\Delta t \geq 0.72$ ps, as manifested by the more pronounced damping in the experiment, to damping factors neglected in the hydrodynamic model such as surface recombination and electron−electron scattering. The latter is particularly relevant at the high pump fluences used in our experiment.[44]

The reconstructed net charge distribution penetrates up to a depth of ∼500 nm inside the crystal bulk (along the *x* axis) and exhibits multiple time-varying annular patterns, visible in both the *xy* and *yz* planes, as illustrated in Figure 3 (see also insets in Figure 2B, and Movie S3). Annular patterns in the *yz* plane are produced by local variations in the excited charge carrier density, owing to the Gaussian profile of the pump laser. The varying charge distribution along such a profile causes changes in the back-and-forth (*x* axis) oscillation frequency and

https://doi.org/10.1021/acsnano.2c10481
ACS Nano 2023, 17, 3645−3656

intensity at each point along the *yz* plane. These intricate oscillations comprise the microscopic features of the photo-Dember effect in the semiconductor, which result in the emission of a composite THz pulse emerging as the superposition of contributions from different points along the surface. In this manner, CDEM allows us to probe the microscopic details behind the generation of single-cycle THz pulses and to follow their evolution in the near field, thus providing understandings on the underlying charge carrier dynamics.

Our model deals with the net current and charge density. While being more compact, this requires to take some care when analyzing and drawing conclusions. Observing Figure 3 and the insets in Figure 2B, at early time delays ($0 \leq \Delta t \leq 0.36$ ps) we see rapid diffusion of electrons into the bulk, while the holes remain near the crystal surface. At later time delays ($0.48 \leq \Delta t \leq 0.72$ ps), we see a partial revival of the electron population near the crystal surface due to the drift force acting on the electrons, pulling them back toward the surface. In the final stage ($0.84 \leq \Delta t \leq 0.96$ ps), we observe once more the diffusion of the electron population toward the bulk. If we track only the hole population, we see that, overall, it continuously diffuses toward the bulk (in each panel the black area gets larger and dimmer in a monotonic fashion). This different behavior between electron and hole dynamics is a direct consequence of the difference in effective mass (or mobility).

Although InAs-based devices are well-developed for applications, to the best of our knowledge, these spatiotemporal and spectral features have never been observed. Our experiment shows how the emitted-field phase front can be controlled by a combination of sample geometry and local pump laser intensity. The intricate dynamics of the charge distribution is manifested by the expanding double-lobe feature exhibited by the emitted THz field, which is clearly discernible in the electron energy-shift maps of Figure 2 for time delays $\Delta t \geq 0.24$ ps. Another signature of the charge distribution is the apparent jump in the THz field phase observed in the energy shift maps around the tip of the triangle-shaped crystal, associated with charge accumulation at the tip and the transition from one side of the dipole to the other. These features illustrate that the emitted field displays a complex spatiotemporal pattern that cannot be explained by a simple dipole model, which is often sufficient for explaining far-field measurements. Such fine features are only resolved by near-field measurements. This is highlighted in Figure 2C, which presents measured spatiotemporal maps of the mean electron energy shifts $\Delta\varepsilon$ in a 5×5 μm^2 region around the crystal tip, demonstrating 50 nm resolution in the *xy*-plane.

We note that further improving the spatial resolution of CDEM is straightforward using state-of-the-art scanning transmission electron microscopy, with two main considerations: (1) Better spatial resolution scales with a smaller field-of-view, as in Figure 2C. (2) For thick samples as used in our experiment, the resolution is limited by the electron beam divergence. For example, an electron beam focused to 10 nm with a convergence angle of 1 milliradian will expand to 110 nm for a 100 μm thick sample. Ultimately, for a conventional TEM sample (about 100 nm thick or less), spatial resolution <1 nm would be achievable, provided that strong enough THz fields are created by the charge dynamics to provide sufficient contrast. Under such a condition, the resolution is far less affected by the electron beam divergence, which is currently the main bottleneck for improving resolution (Figure 2C). In addition, such a thin sample can be penetrated by the electrons, thereby allowing more direct access to the charge dynamics inside the material. The ability to directly access such *bulk* dynamics is a potential major advantage of CDEM for imaging nanoscale charge dynamics, especially when compared to other near-field techniques that are mostly surface-oriented (i.e., sensitive only to the outermost atomic layers of the target material.[2−13]

The underlying mechanism in CDEM is the inelastic scattering of the free-electron pulse off the charges generated in the probed material, mediated by the THz near field produced by the dynamics of such charges. Thus, each pixel in Figure 2 depicts the mean electron energy gain or loss extracted from captured time series of electron energy spectra as illustrated in Figure 4A. Panels in this figure reveal temporal oscillations and broadening of the electron spectra. Tracking the mean electron energy, one can discern a net energy loss followed by a net gain, with feature strengths depending on the pump-laser pulse energy. Importantly, such features in the electron energy spectrum have not been reported in any previous UTEM experiment to the best of our knowledge.

To better understand the physical origin of the features observed in the electron spectrum, we go back to Figure 1B, where we observed three possible electron trajectories labeled Δt_{1-3}. An electron arriving at $\Delta t_1 < 0$ will undergo a small energy shift, despite arriving before the pump laser, owing to the extended nature of the free-electron pulse and interaction region. An electron arriving at $\Delta t_2 \approx 0$ (i.e., around the time of laser-electron overlap) undergoes a strong and abrupt energy shift, as only a certain portion of that extended electron interacts with the THz field generated during its flight. This abrupt change in energy involves high-frequency THz components and, hence, leads to the apparent smearing of the electron spectra in that region. Electrons arriving at $\Delta t_3 > 0$ average over the more slowly varying THz field and, therefore, accelerate or decelerate as a whole depending on the exact time of arrival.

Figure 4B illustrates the excellent agreement obtained between the measured and simulated mean electron energy shifts extracted from the electron spectra in Figure 4A. The mean electron energy shift is simply the average of each spectrum at each time delay. The inverse transition, from the one-dimensional data set $\Delta\varepsilon(\Delta t)$ (as obtained from the classical CDEM theory) to the simulated spectra shown in Figure 4A (bottom panels), is achievable through a convolution with a kernel in two-dimensional energy-shift and time-delay space, representing the free-electron phase-space prior to the interaction with the THz field. Figure 4C compares the measured and simulated peak-to-valley electron energy shifts derived from the data in Figure 4B for different pump pulse energies, showing a saturation at high pulse energies, which stems from the limited achievable photoexcited charge-carrier density.

Figure 5 presents an analysis of the spatial dependence of the reconstructed field, showing that the THz spectrum varies with distance from the sample edge, an effect that is observed only in near-field measurements. In particular, Figure 5A depicts the mean electron energy shift as a function of electron-beam position along *x* and time delay for several pump pulse energies, as extracted from the spatiotemporal maps in Figure 2. The right panels show cross-sections along *x* at the time

https://doi.org/10.1021/acsnano.2c10481
ACS Nano 2023, 17, 3645−3656

delay of maximal energy shift, together with the corresponding simulated cross-sections.

Figures 5B and C show the Fourier transform of both the measured and simulated mean electron-energy shift data displayed in Figure 5A. It is clear that the spectra become narrower as the distance from the crystal grows, a feature that can be traced back to the decay of higher-frequency nonpropagating waves in the near field. The observed spectral bandwidth is in principle limited by the electron pulse duration (~350 fs). However, this bandwidth is still sufficient to perform the current measurement, as shown in Figures 5B and C. Shorter electron pulses should extend the bandwidth even further.

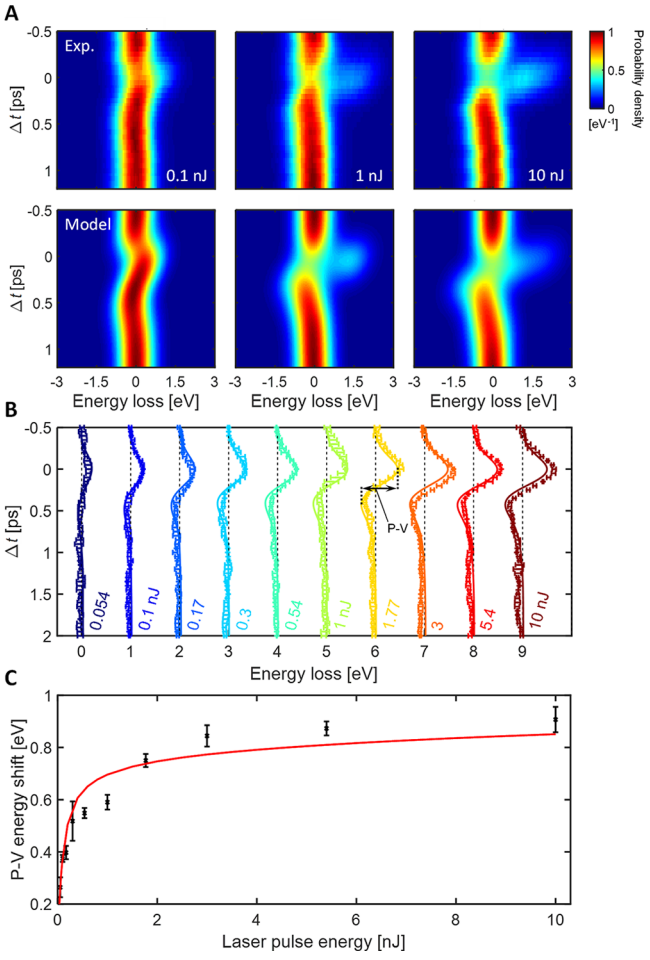

Figure 4. Extracting the temporal dynamics of the THz field from the free-electron–field interaction. (A) Measured (top) and simulated (bottom) electron energy spectra versus time delay for several pump-laser pulse energies. Colors indicate the energy probability density, separately normalized at each time delay. Data were collected with the electron beam passing 1 μm away from the crystal face. (B) Mean electron energy shift extracted from (A) as a function of time delay. Error bars and lines denote experimental and simulated results, respectively. A horizontal offset is introduced for clarity. (C) Peak-to-valley (P–V) electron energy shift (see illustration in (B)) versus pump-laser pulse energy corresponding to the data in (B) (symbols), showing a good agreement with theory (solid curve, see the SI). A common parameter set in the theory matches all data points, for all pulse energies and time delays.

Taking a wider perspective, we note that all electron–field interactions harnessed in electron microscopy can be categorized using three parameters: the field cycle, the electron pulse duration, and the interaction duration L/v (determined by the length of the interaction region L and the electron velocity v). These parameters allow us to classify all electron–field interactions into three regimes. [1] On the one extreme, for a field cycle much shorter than the electron pulse duration, we are in the realm of photon-induced near-field electron microscopy (PINEM).[45−52] [2] The opposite extreme, having a field cycle much longer than both the interaction duration and the electron pulse duration, is the regime of deflectometry,[27−29] holography,[53] and Lorentz transmission electron microscopy[54] (more details on the comparison in the SI). [3] The intermediate regimes (e.g., for a field cycle longer than the electron pulse duration, yet shorter than the interaction time) are where CDEM belongs.

Our CDEM experiment fundamentally differs from previous PINEM experiments both in its time scale (i.e., we operate in regime [3] rather than [1]) and in its intrinsically nonlinear nature associated with the THz field generation starting from infrared laser light. Namely, in our specific demonstration of CDEM, the electron interacts with a field of a much smaller frequency (THz) than the excitation frequency (optical), created due to the optical nonlinearity induced by the charge dynamics (through the photo-Dember effect). Such nonlinear interactions have not been reported in previous PINEM experiments. CDEM can also occur without nonlinearity, by a direct THz excitation, and yet to the best of our knowledge, no realization of CDEM has been previously reported.

Building on previous theoretical developments,[46,47,50,51,55] we formulate a theory for CDEM (see the SI). The CDEM theory goes beyond the coherent narrow-band fields commonly employed in PINEM, and can also accommodate a general electromagnetic potential term to account for incoherent and stochastic processes, as often required to characterize complex charge dynamics. This unified quantum theory thus captures both PINEM (regime [1]) and CDEM (regime [3]) on the same footing. The classical limit of this theory is sufficient when the electron pulse duration is substantially shorter than the field cycle, so the electron can be treated as a point particle. In the present instance, the electron pulse duration is comparable to the field cycle, and therefore, we use the unified quantum theory. Nevertheless, we note that the classical theory also provides a good fit in our case, and thus, we do not claim that the quantum features of the electron are necessary to describe our results.

To estimate the prospects of CDEM for the study of other solid-state phenomena, a useful figure of merit is the instantaneous local current I associated with the observed physics (see theory in the SI). This current is proportional to the force acting on the probe electron, which in turn produces the electron energy shifts. Based on both measurements and simulations, the lower limit that is observable for this figure of merit using the current setup is $\sim 10^{-2}$ A, corresponding to a ~0.1 eV energy shift (see theory in the SI). This current is equivalent to $\sim 10^{5}$ electrons undergoing picosecond-scale dynamics. Higher-resolution electron spectrometers that are commercially available can reduce this value by 2 orders of magnitude.[43]

These estimates show that CDEM can probe previously inaccessible dynamics, such as the ultrafast nature of superconducting phase transitions,[56,57] recording the forma-

https://doi.org/10.1021/acsnano.2c10481
ACS Nano 2023, 17, 3645−3656

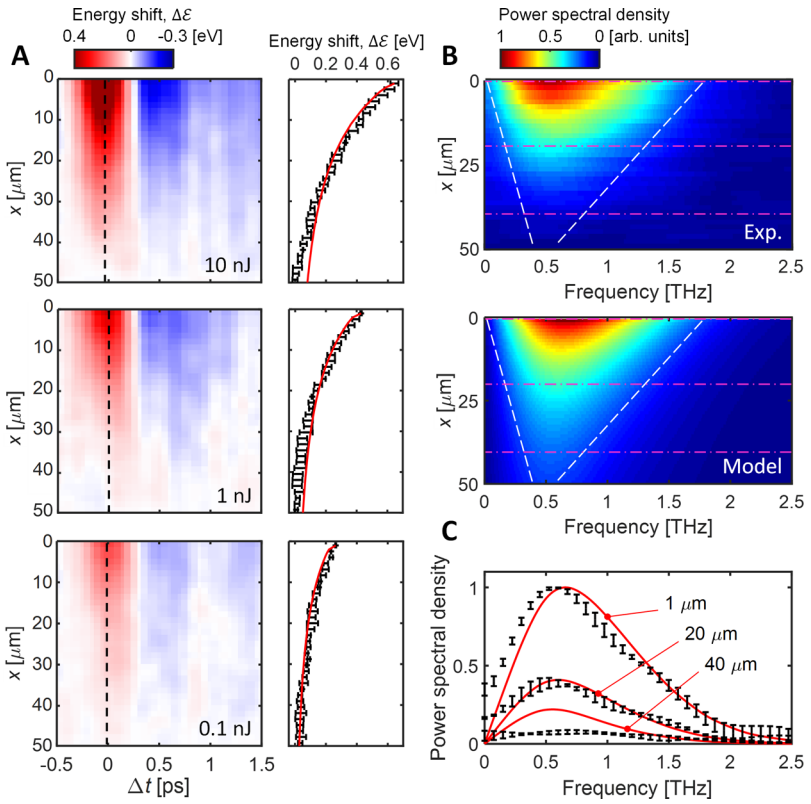

Figure 5. Mapping the spectrum of the THz near field. (A) Mean electron energy shift $\Delta\varepsilon$ as a function of pump−probe time delay and position along the x coordinate, normal to the crystal face. Data were collected by scanning the electron beam position along the direction of pump-laser incidence x, with $x = 0$ at the crystal surface. The color bar has 30% saturation for better visibility. Right panels show a comparison with theory (solid curves) taken at the time delay of maximal energy shift (as indicated by the vertical dashed lines in the left panels). (B) Measured (top) and simulated (bottom) power spectral density maps versus position along x, as obtained from $\Delta\varepsilon$. White dashed lines illustrate a spectra narrowing with increasing distance from the crystal. (C) Cross-sections of the measured (black error bars) and simulated (red curves) data presented in (B), taken at various x positions (indicated by horizontal magenta lines in (B)). The pump-laser pulse energy in (B) and (C) is 10 nJ.

tion and resolving the core dynamics of nanoscale vortices in type-II superconductors with nanometer imaging resolution. Here, we provide an estimate for the feasibility of this idea by considering the instantaneous local current I associated with the switching on/off of a vortex of a single magnetic flux quantum using a femtosecond laser pulse.[58] Detailed calculations and a roadmap toward such an experiment are provided in the SI. As a concrete example, consider a vortex tube of a single flux quantum, trapped in a type-II superconductor. Such a vortex is surrounded by a current loop with a typical strength of 10^{-3} A,[59] thus anticipating a 10-meV-scale energy shift, which is measurable using state-of-the-art electron spectrometers.[43] Recalling the known 1−10 ps time scale for this optically driven phase transition,[57] we conclude that the sensitivity of CDEM is sufficient to provide detailed spatiotemporal imaging of this effect (more information in the SI).

Looking forward, CDEM experiments utilizing field cycles ranging between ∼100 fs and ∼10 ps are readily achievable using the current setup. Importantly, this time frame is relevant for many physical phenomena of interest and can be tuned by changing the size of the interaction region or the electron velocity (affecting both the electron pulse duration and its interaction time). Intriguingly, the ∼100 fs lower limit could be made 3 orders of magnitude shorter using attosecond electron pulse trains.[60−62]

CONCLUSIONS

In conclusion, CDEM offers a sensitive nonperturbing probe to explore the dynamics of charge carriers inside matter with nanometer-femtosecond spatiotemporal resolution. Our experiment elucidates the intricate electron−hole dynamics taking place inside a photoexcited InAs crystal. The ability to image ultrafast charge dynamics in different materials can assist in future designs of ultrafast nanostructured devices by, for example, optimizing the performance of THz electronics or controlling the beam phase front of metasurface-based THz sources. On a more fundamental level, we expect the CDEM technique to be well-suited to provide quantitative information on the angular distribution of the Fermi velocity of charge carriers in solids−mapping the 3D Fermi surface. This way, CDEM may provide a dynamical nanoscale-resolved alternative to the de Haas−Van Alphen effect.[63−65]

In general, wherever one has a spatially textured distribution of charge carriers evolving in time and space, like we have in the photo-Dember effect, CDEM can record the associated ultrafast microscopic features. For example, CDEM can facilitate the exploration of hot-carrier dynamics in metals and nano-optoelectronic devices,[66−69] as well as transport effects related to the magnetoresistance[70,71] and Hall[72,73] effects. These phenomena can be explored in a time-resolved manner to provide insights into their nature. A similar approach as applied in our experiment could record the

https://doi.org/10.1021/acsnano.2c10481
ACS Nano 2023, 17, 3645−3656

dynamics of light-induced superconductivity,[57,58] alongside other types of light-induced phase transitions such as those involving charge density waves, the quantum spin Hall effect, and the quantum anomalous Hall effect. Besides phase transitions, one could explore other light-induced phenomena,[74] including ultrafast interlayer charge transfer in heterostructures of transition metal dichalcogenides (TMDs),[75] the light-induced anomalous Hall effect, the photovoltaic Hall effect, and ultrafast aspects of Floquet engineering. In all these instances, CDEM could grant us access into the microscopic out-of-equilibrium dynamics of charge carriers to map their spatial dependences, as demonstrated in our experiment with the photo-Dember effect.

METHODS

Experimental Setup: Ultrafast Transmission Electron Microscope (UTEM). The experiments are conducted using a Jeol 2100 Plus transmission electron microscope (TEM) equipped with a LaB_6 electron gun and driven by femtosecond laser pulses, thus operating as an ultrafast transmission electron microscope (UTEM), as illustrated in Figure 6. In the UTEM, a laser pump pulse excites the sample, and an electron probe pulse records the transient state of the specimen. The pump and probe pulses are created by a 1030 nm, ~220 fs laser (Carbide, Light Conversion) operating at a 1 MHz repetition rate. Each pulse is split into two: The first pulse is up-converted to UV via two stages of second-harmonic generation and then guided to the TEM cathode by an aluminum mirror inserted inside the TEM column. This process generates femtosecond electron pulses at the laser repetition rate. The electron pulses are accelerated to 200 keV and travel down the TEM column, passing by the vicinity of the sample and providing imaging or spectroscopic information, just as in a conventional TEM. The second pulse is converted to 800 nm wavelength and 50 fs pulse duration (FWHM) using an optical parametric amplifier (OPA) and a pulse compressor. This pulse is then used to pump the sample, impinging on it from the side (relative to the electron beam), where the laser spot size is 40 μm FWHM. The time delay between electron-probe and laser-pump pulses is controlled by a motorized stage, thus allowing for stroboscopic measurements of femtosecond dynamics.

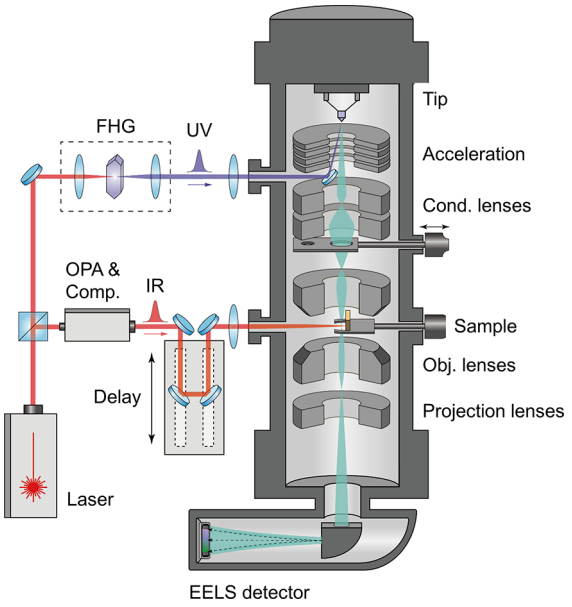

Figure 6. Experimental setup: ultrafast transmission electron microscope (UTEM). Illustration of an ultrafast transmission electron microscope (UTEM), depicting the UV and IR laser paths, and the TEM column. FHG, fourth harmonic generation; OPA, optical parametric amplifier; Comp., laser pulse compressor; Cond., condenser; Obj., objective.

Electron Spectroscopy in Scanning Transmission Electron Microscopy (STEM-EELS) Mode. To analyze the electron (kinetic energy) spectrum after interaction with the sample, a postcolumn electron energy-loss spectroscopy (EELS) system (by Gatan) is installed in the TEM. The EELS data can be captured at each xy (lateral) position within the field of view (FOV) using the built-in scanning TEM (STEM) capability (see Figure 1). We perform experiments with several FOVs and electron spot sizes. The results presented in Figure 2A (2C) are acquired with a FOV of 120 × 120 μm^2 (5 × 5 μm^2) and an electron lateral spot size of 1 μm (50 nm) FWHM. The STEM electron lens system is tuned to collimate the electron, so it maintains this spot size along the entire length of the interaction region.

In order to collect the data shown in Figures 2 and 5, the STEM-EELS measurement is repeated for several pump−probe time delays and pulse energies, generating a five-dimensional hypercube of EELS data (with the dimensions being x, y, energy, time delay, and pulse energy).

Sample Preparation. The sample used in our experiments was prepared from a p-type (10^{17} cm^{-3}) 500 μm-thick single crystal InAs wafer with (111) growth orientation (from MTI Corp.). A piece from the wafer was manually thinned and polished to 60 μm using standard TEM sample preparation techniques. The thinned crystal was then cleaved along the {110} planes and glued to a TEM copper grid before being mounted on the TEM holder.

In order to demonstrate the 50 nm spatial resolution of Figure 2C, a 10 × 10 μm^2 area around the InAs crystal tip was further thinned to a final thickness of 20 μm using focused ion beam milling (FEI Helios NanoLab DualBeam G3 UC). This thinning relaxes the constraint imposed by the electron beam divergence, as the distance (in z) along which the beam diameter must be retained is significantly reduced.

Several different samples were used in our measurements, all showing similar behavior. The experimental data presented in the main text were collected from a single sample.

ASSOCIATED CONTENT

Supporting Information

The Supporting Information is available free of charge at https://pubs.acs.org/doi/10.1021/acsnano.2c10481.

Theory of CDEM; comparison of CDEM to other regimes of electron−field interactions; hydrodynamic model of photo-Dember effect; complete model for electron−field interaction, also considering the triangular sample geometry; different sample geometries considered in our experiment; general principles for sensitivity of CDEM: guidelines for applications in other systems; spatiotemporal maps of electron energy shifts for straight-edge sample geometry; spatiotemporal maps of electron energy shifts focusing on InAs crystal tip (PDF)

Spatiotemporal maps of electron energy shifts for triangular geometry (MPG)

Spatiotemporal maps of electron energy shifts for straight-edge geometry (MPG)

Spatiotemporal evolution of reconstructed charge density (MPG)

AUTHOR INFORMATION

Corresponding Author

Ido Kaminer − *Technion - Israel Institute of Technology, Haifa 3200003, Israel;* orcid.org/0000-0003-2691-1892; Email: kaminer@technion.ac.il

https://doi.org/10.1021/acsnano.2c10481
ACS Nano 2023, 17, 3645−3656

Authors

Michael Yannai − *Technion - Israel Institute of Technology, Haifa 3200003, Israel;* orcid.org/0000-0002-8482-1871

Raphael Dahan − *Technion - Israel Institute of Technology, Haifa 3200003, Israel*

Alexey Gorlach − *Technion - Israel Institute of Technology, Haifa 3200003, Israel*

Yuval Adiv − *Technion - Israel Institute of Technology, Haifa 3200003, Israel;* orcid.org/0000-0002-7451-4130

Kangpeng Wang − *Technion - Israel Institute of Technology, Haifa 3200003, Israel*

Ivan Madan − *Institute of Physics, École Polytechnique Fédérale de Lausanne, Lausanne 1015, Switzerland;* orcid.org/0000-0002-0137-8537

Simone Gargiulo − *Institute of Physics, École Polytechnique Fédérale de Lausanne, Lausanne 1015, Switzerland;* orcid.org/0000-0002-7820-3372

Francesco Barantani − *Institute of Physics, École Polytechnique Fédérale de Lausanne, Lausanne 1015, Switzerland; Department of Quantum Matter Physics, University of Geneva, 1211 Geneva 4, Switzerland;* orcid.org/0000-0002-2053-1365

Eduardo J. C. Dias − *ICFO-Institut de Ciencies Fotoniques, The Barcelona Institute of Science and Technology, 08860 Castelldefels, Barcelona, Spain*

Giovanni Maria Vanacore − *Department of Materials Science, University of Milano-Bicocca, 20121 Milano, Italy;* orcid.org/0000-0002-7228-7982

Nicholas Rivera − *Massachusetts Institute of Technology, Cambridge, Massachusetts 02139, United States;* orcid.org/0000-0002-8298-1468

Fabrizio Carbone − *Institute of Physics, École Polytechnique Fédérale de Lausanne, Lausanne 1015, Switzerland*

F. Javier García de Abajo − *ICFO-Institut de Ciencies Fotoniques, The Barcelona Institute of Science and Technology, 08860 Castelldefels, Barcelona, Spain; ICREA-Institució Catalana de Recerca i Estudis Avançats, 08010 Barcelona, Spain;* orcid.org/0000-0002-4970-4565

Complete contact information is available at: https://pubs.acs.org/10.1021/acsnano.2c10481

Notes

We note that a parallel work (Madan et al., "Charge dynamics electron microscopy: nanoscale imaging of femtosecond plasma dynamics") has simultaneously demonstrated CDEM in a different field, for the visualization of charged plasma dynamics in a UTEM. The first preliminary results of both papers were first presented as two abstracts in CLEO 2021.[76,77] The preprint version of this paper is available on arXiv: Yannai, M.; Dahan, R.; Gorlach, A.; Adiv, Y.; Wang, K.; Madan, I.; Gargiulo, S.; Barantani, F.; Dias, E. J. C.; Vanacore, G. M.; Rivera, N.; Carbone, F.; García de Abajo, F. J.; Kaminer, I. Ultrafast Electron Microscopy of Nanoscale Charge Dynamics in Semiconductors. 2022, arXiv:2206.02556. https://arxiv.org/ftp/arxiv/papers/2206/2206.02556.pdf (accessed January 24, 2023).

The authors declare no competing financial interest.

ACKNOWLEDGMENTS

The research was supported by the European Research Council (ERC Advanced Grant 789104-eNANO and ERC Starting Grant 851780-NanoEP), the European Union (Horizon 2020 Research and Innovation Program under grant agreement No. 964591 SMART-electron), the Spanish MICINN (PID2020-112625GB-I00 and Severo Ochoa CEX2019-000910-S), the Catalan CERCA Program, and Fundaciós Cellex and Mir-Puig. We thank T. Ellenbogen, E. Yalon, and D. Ritter for their support, advice, and helpful discussions. We thank Y. Kauffmann and C. Dickinson for their assistance and advice in STEM operation. We are also grateful to M. Kalina and G. Atiya for assistance in the sample preparation. The experiments were performed on the UTEM of the AdQuanta group of I. K., which is installed in the electron microscopy center (MIKA) of the Department of Materials Science and Engineering at Technion. M. Y. and R. D. are partially supported by the VATAT Quantum Science and Technology scholarship.

REFERENCES

(1) Lloyd-Hughes, J.; Oppeneer, P. M.; Pereira Dos Santos, T.; Schleife, A.; Meng, S.; Sentef, M. A.; Ruggenthaler, M.; Rubio, A.; Radu, I.; Murnane, M.; Shi, X.; Kapteyn, H.; Stadtmüller, B.; Dani, K. M.; da Jornada, F. H.; Prinz, E.; Aeschlimann, M.; Milot, R. L.; Burdanova, M.; Boland, J.; et al. The 2021 Ultrafast Spectroscopic Probes of Condensed Matter Roadmap. *J. Phys.: Condens. Matter* **2021**, *33*, 353001.

(2) Chen, X.; Hu, D.; Mescall, R.; You, G.; Basov, D. N.; Dai, Q.; Liu, M. Modern Scattering-Type Scanning Near-Field Optical Microscopy for Advanced Material Research. *Adv. Mater.* **2019**, *31*, 1804774.

(3) Atkin, J. M.; Berweger, S.; Jones, A. C.; Raschke, M. B. Nano-Optical Imaging and Spectroscopy of Order, Phases, and Domains in Complex Solids. *Adv. Phys.* **2012**, *61*, 745−842.

(4) Rudolf, D.; La-O-Vorakiat, C.; Battiato, M.; Adam, R.; Shaw, J. M.; Turgut, E.; Maldonado, P.; Mathias, S.; Grychtol, P.; Nembach, H. T.; Silva, T. J.; Aeschlimann, M.; Kapteyn, H. C.; Murnane, M. M.; Schneider, C. M.; Oppeneer, P. M. Ultrafast Magnetization Enhancement in Metallic Multilayers Driven by Superdiffusive Spin Current. *Nat. Commun.* **2012**, *3*, 1037.

(5) Miao, J.; Ishikawa, T.; Robinson, I. K.; Murnane, M. M. Beyond Crystallography: Diffractive Imaging Using Coherent x-Ray Light Sources. *Science* **2015**, *348*, 530−535.

(6) Wieghold, S.; Nienhaus, L. Probing Semiconductor Properties with Optical Scanning Tunneling Microscopy. *Joule* **2020**, *4*, 524−538.

(7) Bauer, M.; Aeschlimann, M. Dynamics of Excited Electrons in Metals, Thin Films and Nanostructures. *J. Electron Spectrosc. Relat. Phenom.* **2002**, *124*, 225−243.

(8) Spektor, G.; Kilbane, D.; Mahro, A. K.; Frank, B.; Ristok, S.; Gal, L.; Kahl, P.; Podbiel, D.; Mathias, S.; Giessen, H.; Meyer Zu Heringdorf, F.-J.; Orenstein, M.; Aeschlimann, M. Revealing the Subfemtosecond Dynamics of Orbital Angular Momentum in Nanoplasmonic Vortices. *Science* **2017**, *355*, 1187−1191.

(9) Stolow, A.; Bragg, A. E.; Neumark, D. M. Femtosecond Time-Resolved Photoelectron Spectroscopy. *Chem. Rev.* **2004**, *104*, 1719−1757.

(10) Smallwood, C. L.; Kaindl, R. A.; Lanzara, A. Ultrafast Angle-Resolved Photoemission Spectroscopy of Quantum Materials. *Europhys. Lett.* **2016**, *115*, 27001.

(11) Krömker, B.; Escher, M.; Funnemann, D.; Hartung, D.; Engelhard, H.; Kirschner, J. Development of a Momentum Microscope for Time Resolved Band Structure Imaging. *Rev. Sci. Instrum.* **2008**, *79*, 053702.

(12) Tusche, C.; Krasyuk, A.; Kirschner, J. Spin Resolved Bandstructure Imaging with a High Resolution Momentum Microscope. *Ultramicroscopy* **2015**, *159*, 520−529.

(13) Najafi, E.; Scarborough, T. D.; Tang, J.; Zewail, A. Four-Dimensional Imaging of Carrier Interface Dynamics in p-n Junctions. *Science* **2015**, *347*, 164−167.

(14) Ulbricht, R.; Hendry, E.; Shan, J.; Heinz, T. F.; Bonn, M. Carrier Dynamics in Semiconductors Studied with Time-Resolved Terahertz Spectroscopy. *Rev. Mod. Phys.* **2011**, *83*, 543−586.
(15) Cocker, T. L.; Jelic, V.; Gupta, M.; Molesky, S. J.; Burgess, J. A. J.; Reyes, G. D. L.; Titova, L. v.; Tsui, Y. Y.; Freeman, M. R.; Hegmann, F. A. An Ultrafast Terahertz Scanning Tunnelling Microscope. *Nat. Photonics* **2013**, *7*, 620−625.
(16) Klarskov, P.; Kim, H.; Colvin, V. L.; Mittleman, D. M. Nanoscale Laser Terahertz Emission Microscopy. *ACS Photonics* **2017**, *4*, 2676−2680.
(17) Baum, P.; Yang, D.-S.; Zewail, A. H. 4D Visualization of Transitional Structures in Phase Transformations by Electron Diffraction. *Science* **2007**, *318*, 788−792.
(18) Morrison, V. R.; Chatelain, R. P.; Tiwari, K. L.; Hendaoui, A.; Bruhács, A.; Chaker, M.; Siwick, B. J. A Photoinduced Metal-like Phase of Monoclinic VO_2 Revealed by Ultrafast Electron Diffraction. *Science* **2014**, *346*, 445−448.
(19) Kogar, A.; Zong, A.; Dolgirev, P. E.; Shen, X.; Straquadine, J.; Bie, Y. Q.; Wang, X.; Rohwer, T.; Tung, I. C.; Yang, Y.; Li, R.; Yang, J.; Weathersby, S.; Park, S.; Kozina, M. E.; Sie, E. J.; Wen, H.; Jarillo-Herrero, P.; Fisher, I. R.; Wang, X.; et al. Light-Induced Charge Density Wave in $LaTe_3$. *Nat. Phys.* **2020**, *16*, 159−163.
(20) Otto, M. R.; Pöhls, J.-H.; René de Cotret, L. P.; Stern, M. J.; Sutton, M.; Siwick, B. J. Mechanisms of Electron-Phonon Coupling Unraveled in Momentum and Time: The Case of Soft Phonons in $TiSe_2$. *Sci. Adv.* **2021**, *7*, No. eabf2810.
(21) Quinonez, E.; Handali, J.; Barwick, B. Femtosecond Photoelectron Point Projection Microscope. *Rev. Sci. Instrum.* **2013**, *84*, 103710.
(22) Müller, M.; Paarmann, A.; Ernstorfer, R. Femtosecond Electrons Probing Currents and Atomic Structure in Nanomaterials. *Nat. Commun.* **2014**, *5*, 5292.
(23) Vogelsang, J.; Hergert, G.; Wang, D.; Groß, P.; Lienau, C. Observing Charge Separation in Nanoantennas via Ultrafast Point-Projection Electron Microscopy. *Light: Sci. Appl.* **2018**, *7*, 55.
(24) Hergert, G.; Wöste, A.; Vogelsang, J.; Quenzel, T.; Wang, D.; Gross, P.; Lienau, C. Probing Transient Localized Electromagnetic Fields Using Low-Energy Point-Projection Electron Microscopy. *ACS Photonics* **2021**, *8*, 2573−2580.
(25) Hachtel, J. A.; Idrobo, J. C.; Chi, M. Sub-Ångstrom Electric Field Measurements on a Universal Detector in a Scanning Transmission Electron Microscope. *Adv. Struct. Chem. Imaging* **2018**, *4*, 1−10.
(26) Kohno, Y.; Seki, T.; Findlay, S. D.; Ikuhara, Y.; Shibata, N. Real-Space Visualization of Intrinsic Magnetic Fields of an Antiferromagnet. *Nature* **2022**, *602*, 234−239.
(27) Ryabov, A.; Baum, P. Electron Microscopy of Electromagnetic Waveforms. *Science* **2016**, *353*, 374−377.
(28) Sun, S.; Sun, X.; Bartles, D.; Wozniak, E.; Williams, J.; Zhang, P.; Ruan, C. Y. Direct Imaging of Plasma Waves Using Ultrafast Electron Microscopy. *Struct. Dyn.* **2020**, *7*, 064301.
(29) Centurion, M.; Reckenthaeler, P.; Trushin, S. A.; Krausz, F.; Fill, E. E. Picosecond Electron Deflectometry of Optical-Field Ionized Plasmas. *Nat. Photonics* **2008**, *2*, 315−318.
(30) Zewail, A. H. Four-Dimensional Electron Microscopy. *Science* **2010**, *328*, 187−193.
(31) Talebi, N. Interaction of Electron Beams with Optical Nanostructures and Metamaterials: From Coherent Photon Sources towards Shaping the Wave Function. *J. Opt.* **2017**, *19*, 103001.
(32) Piazza, L.; Lummen, T. T. A.; Quiñonez, E.; Murooka, Y.; Reed, B. W.; Barwick, B.; Carbone, F. Simultaneous Observation of the Quantization and the Interference Pattern of a Plasmonic Near-Field. *Nat. Commun.* **2015**, *6*, 6407.
(33) Lummen, T. T. A.; Lamb, R. J.; Berruto, G.; Lagrange, T.; Dal Negro, L.; García de Abajo, F. J.; McGrouther, D.; Barwick, B.; Carbone, F. Imaging and Controlling Plasmonic Interference Fields at Buried Interfaces. *Nat. Commun.* **2016**, *7*, 13156.
(34) Kfir, O.; Lourenço-Martins, H.; Storeck, G.; Sivis, M.; Harvey, T. R.; Kippenberg, T. J.; Feist, A.; Ropers, C. Controlling Free Electrons with Optical Whispering-Gallery Modes. *Nature* **2020**, *582*, 46−49.
(35) Wang, K.; Dahan, R.; Shentcis, M.; Kauffmann, Y.; Ben Hayun, A.; Reinhardt, O.; Tsesses, S.; Kaminer, I. Coherent Interaction between Free Electrons and a Photonic Cavity. *Nature* **2020**, *582*, 50−54.
(36) Fishman, T.; Haeusler, U.; Dahan, R.; Yannai, M.; Adiv, Y.; Lenkiewicz Abudi, T.; Shiloh, R.; Eyal, O.; Yousefi, P.; Eisenstein, G.; Hommelhoff, P.; Kaminer, I. Imaging the Field inside Nanophotonic Devices. *arXiv:2209.13960*, 2022. https://arxiv.org/ftp/arxiv/papers/2209/2209.13960.pdf (accessed 01-24-2023).
(37) Cremons, D. R.; Plemmons, D. A.; Flannigan, D. J. Femtosecond Electron Imaging of Defect-Modulated Phonon Dynamics. *Nat. Commun.* **2016**, *7*, 11230.
(38) Kurman, Y.; Dahan, R.; Herzig Sheinfux, H.; Wang, K.; Yannai, M.; Adiv, Y.; Reinhardt, O.; G Tizei, L. H.; Woo, S. Y.; Li, J.; Edgar, J. H.; Kociak, M.; L Koppens, F. H.; Kaminer, I. Spatiotemporal Imaging of 2D Polariton Wave Packet Dynamics Using Free Electrons. *Science* **2021**, *372*, 1181−1186.
(39) Fu, X.; Barantani, F.; Gargiulo, S.; Madan, I.; Berruto, G.; LaGrange, T.; Jin, L.; Wu, J.; Vanacore, G. M.; Carbone, F.; Zhu, Y. Nanoscale-Femtosecond Dielectric Response of Mott Insulators Captured by Two-Color Near-Field Ultrafast Electron Microscopy. *Nat. Commun.* **2020**, *11*, 5770.
(40) Danz, T.; Domröse, T.; Ropers, C. Ultrafast Nanoimaging of the Order Parameter in a Structural Phase Transition. *Science* **2021**, *371*, 371−374.
(41) Berruto, G.; Madan, I.; Murooka, Y.; Vanacore, G. M.; Pomarico, E.; Rajeswari, J.; Lamb, R.; Huang, P.; Kruchkov, A. J.; Togawa, Y.; LaGrange, T.; McGrouther, D.; Rønnow, H. M.; Carbone, F. Laser-Induced Skyrmion Writing and Erasing in an Ultrafast Cryo-Lorentz Transmission Electron Microscope. *Phys. Rev. Lett.* **2018**, *120*, 117201.
(42) Dember, H. Photoelectromotive force in cuprous oxide crystals. *Phys. Z.* **1931**, *32*, 554−556.
(43) Krivanek, O. L.; Dellby, N.; Hachtel, J. A.; Idrobo, J. C.; Hotz, M. T.; Plotkin-Swing, B.; Bacon, N. J.; Bleloch, A. L.; Corbin, G. J.; Hoffman, M. V.; Meyer, C. E.; Lovejoy, T. C. Progress in Ultrahigh Energy Resolution EELS. *Ultramicroscopy* **2019**, *203*, 60−67.
(44) Reklaitis, A. Terahertz Emission from InAs Induced by Photo-Dember Effect: Hydrodynamic Analysis and Monte Carlo Simulations. *J. Appl. Phys.* **2010**, *108*, 053102.
(45) Barwick, B.; Flannigan, D. J.; Zewail, A. H. Photon-Induced near-Field Electron Microscopy. *Nature* **2009**, *462*, 902−906.
(46) García de Abajo, F. J.; Asenjo-Garcia, A.; Kociak, M. Multiphoton Absorption and Emission by Interaction of Swift Electrons with Evanescent Light Fields. *Nano Lett.* **2010**, *10*, 1859−1863.
(47) Park, S. T.; Lin, M.; Zewail, A. H. Photon-Induced near-Field Electron Microscopy (PINEM): Theoretical and Experimental. *New J. Phys.* **2010**, *12*, 123028.
(48) García de Abajo, F. J.; Barwick, B.; Carbone, F. Electron Diffraction by Plasmon Waves. *Phys. Rev. B* **2016**, *94*, 041404.
(49) Cai, W.; Reinhardt, O.; Kaminer, I.; García de Abajo, F. J. Efficient Orbital Angular Momentum Transfer between Plasmons and Free Electrons. *Phys. Rev. B* **2018**, *98*, 045424.
(50) Vanacore, G. M.; Madan, I.; Berruto, G.; Wang, K.; Pomarico, E.; Lamb, R. J.; McGrouther, D.; Kaminer, I.; Barwick, B.; García de Abajo, F. J.; Carbone, F. Attosecond Coherent Control of Free-Electron Wave Functions Using Semi-Infinite Light Fields. *Nat. Commun.* **2018**, *9*, 2694.
(51) Reinhardt, O.; Kaminer, I. Theory of Shaping Electron Wavepackets with Light. *ACS Photonics* **2020**, *7*, 2859−2870.
(52) García de Abajo, F. J.; Di Giulio, V. Optical Excitations with Electron Beams: Challenges and Opportunities. *ACS Photonics* **2021**, *8*, 945−974.
(53) Lichte, H.; Lehmann, M. Electron Holography—Basics and Applications. *Rep. Prog. Phys.* **2008**, *71*, 016102.

https://doi.org/10.1021/acsnano.2c10481
ACS Nano 2023, 17, 3645−3656

(54) Phatak, C.; Petford-Long, A. K.; De Graef, M. Recent Advances in Lorentz Microscopy. *Curr. Opin. Solid State Mater. Sci.* **2016**, *20*, 107−114.
(55) Pan, Y.; Zhang, B.; Gover, A. Anomalous Photon-Induced Near-Field Electron Microscopy. *Phys. Rev. Lett.* **2019**, *122*, 183204.
(56) Fausti, D.; Tobey, R. I.; Dean, N.; Kaiser, S.; Dienst, A.; Hoffmann, M. C.; Pyon, S.; Takayama, T.; Takagi, H.; Cavalleri, A. Light-Induced Superconductivity in a Stripe-Ordered Cuprate. *Science* **2011**, *331*, 189−191.
(57) Beck, M.; Klammer, M.; Lang, S.; Leiderer, P.; Kabanov, V. V.; Gol'tsman, G. N.; Demsar, J. Energy-Gap Dynamics of Superconducting NbN Thin Films Studied by Time-Resolved Terahertz Spectroscopy. *Phys. Rev. Lett.* **2011**, *107*, 177007.
(58) Veshchunov, I. S.; Magrini, W.; Mironov, S. v.; Godin, A. G.; Trebbia, J. B.; Buzdin, A. I.; Tamarat, P.; Lounis, B. Optical Manipulation of Single Flux Quanta. *Nat. Commun.* **2016**, *7*, 12801.
(59) Tinkham, M. Magnetic Properties of Classic Type II Superconductors. In*Introduction to Superconductivity*, 2nd ed.; McGraw-Hill: New York, 1996; pp 153−154.
(60) Priebe, K. E.; Rathje, C.; Yalunin, S. V.; Hohage, T.; Feist, A.; Schäfer, S.; Ropers, C. Attosecond Electron Pulse Trains and Quantum State Reconstruction in Ultrafast Transmission Electron Microscopy. *Nat. Photonics* **2017**, *11*, 793−797.
(61) Kozák, M.; Schönenberger, N.; Hommelhoff, P. Ponderomotive Generation and Detection of Attosecond Free-Electron Pulse Trains. *Phys. Rev. Lett.* **2018**, *120*, 103203.
(62) Morimoto, Y.; Baum, P. Diffraction and Microscopy with Attosecond Electron Pulse Trains. *Nat. Phys.* **2018**, *14*, 252−256.
(63) De Haas, W. J.; Van Alphen, P. M. The dependence of the susceptibility of diamagnetic metals upon the field. *Proc. Netherlands R. Acad. Sci.* **1930**, *33*, 170.
(64) Mcclure, J. W. Band Structure of Graphite and de Haas-van Alphen Effect. *Phys. Rev.* **1957**, *108*, 612−618.
(65) Eisenstein, J. P.; Stormer, H. L.; Narayanamurti, V.; Cho, A. Y.; Gossard, A. C.; Tu, C. W. Density of States and de Haas-van Alphen Effect in Two-Dimensional Electron Systems. *Phys. Rev. Lett.* **1985**, *55*, 875−878.
(66) Hohlfeld, J.; Wellershoff, S.-S.; Güdde, J.; Conrad, U.; Jähnke, V.; Matthias, E.; Matthias, M. Electron and Lattice Dynamics Following Optical Excitation of Metals. *Chem. Phys.* **2000**, *251*, 237−258.
(67) Johannsen, J. C.; Ulstrup, S.; Cilento, F.; Crepaldi, A.; Zacchigna, M.; Cacho, C.; Turcu, I. C. E.; Springate, E.; Fromm, F.; Raidel, C.; Seyller, T.; Parmigiani, F.; Grioni, M.; Hofmann, P. Direct View of Hot Carrier Dynamics in Graphene. *Phys. Rev. Lett.* **2013**, *111*, 027403.
(68) Gierz, I.; Petersen, J. C.; Mitrano, M.; Cacho, C.; Turcu, I. C. E.; Springate, E.; Stöhr, A.; Köhler, A.; Starke, U.; Cavalleri, A. Snapshots of Non-Equilibrium Dirac Carrier Distributions in Graphene. *Nat. Mater.* **2013**, *12*, 1119−1124.
(69) Brown, A. M.; Sundararaman, R.; Narang, P.; Goddard, W. A.; Atwater, H. A. Nonradiative Plasmon Decay and Hot Carrier Dynamics: Effects of Phonons, Surfaces, and Geometry. *ACS Nano* **2016**, *10*, 957−966.
(70) Ramirez, A. P. Colossal Magnetoresistance. *J. Phys.: Condens. Matter.* **1997**, *9*, 8171.
(71) Ennen, I.; Kappe, D.; Rempel, T.; Glenske, C.; Hütten, A. Giant Magnetoresistance: Basic Concepts, Microstructure, Magnetic Interactions and Applications. *Sensors* **2016**, *16*, 904.
(72) Novoselov, K. S.; Jiang, Z.; Zhang, Y.; Morozov, S. v.; Stormer, H. L.; Zeitler, U.; Maan, J. C.; Boebinger, G. S.; Kim, P.; Geim, A. K. Room-Temperature Quantum Hall Effect in Graphene. *Science* **2007**, *315*, 1379−1379.
(73) McIver, J. W.; Schulte, B.; Stein, F. U.; Matsuyama, T.; Jotzu, G.; Meier, G.; Cavalleri, A. Light-Induced Anomalous Hall Effect in Graphene. *Nat. Phys.* **2020**, *16*, 38−41.
(74) Bao, C.; Tang, P.; Sun, D.; Zhou, S. Light-Induced Emergent Phenomena in 2D Materials and Topological Materials. *Nat. Rev. Phys.* **2022**, *4*, 33−48.
(75) Ma, E. Y.; Guzelturk, B.; Li, G.; Cao, L.; Shen, Z.-X.; Lindenberg, A. M.; Heinz, T. F. Recording Interfacial Currents on the Subnanometer Length and Femtosecond Time Scale by Terahertz Emission. *Sci. Adv.* **2019**, *5*, No. eaau0073.
(76) Yannai, M.; Dahan, R.; Gorlach, A.; Rivera, N.; Wang, K.; Vanacore, G. M.; Carbone, F.; García de Abajo, F. J.; Kaminer, I. Demonstration of Near-Field THz Spectroscopy Using Ultrafast Electron Microscopy. *Conference on Lasers and Electro-Optics (CLEO)* 2021, SW2K.4.
(77) Gargiulo, S.; Madan, I.; Barantani, F.; Berruto, G.; Yannai, M.; Dias, E. J. C.; Dahan, R.; Kaminer, I.; Vanacore, G. M.; García de Abajo, F. J.; Carbone, F. Charge Dynamics Electron Microscopy; *Conference on Lasers and Electro-Optics (CLEO)* 2021, FM1O.3.

https://doi.org/10.1021/acsnano.2c10481
ACS Nano 2023, 17, 3645−3656